Frontiers of Information Technology & Electronic Engineering
www.jzus.zju.edu.cn; engineering.cae.cn; www.springerlink.com
ISSN 2095-9184 (print); ISSN 2095-9230 (online)
E-mail: jzus@zju.edu.cn

Miniaturized Rotman lens with applications to wireless communication

Bao-hua SUN[†‡], Qiu-yan LIANG, Gao-nan ZHOU

National Key Laboratory of Science and Technology on Antenna and Microwave, Xidian University, Xi'an 710071, China

[†]E-mail: bhsun@mail.xidian.edu.cn

Received Sept. 18, 2019; Revision accepted Dec. 17, 2019; Crosschecked Jan. 19, 2020

Abstract: Rotman lens is a type of beamforming network with many advantages, such as true-time delay characteristic, multibeam capability, and wide bandwidth. Rotman lens has been used in a wide range of applications in today's wireless communication systems. However, the size of a conventional Rotman lens is considerably large. So, difficulties may arise with respect to its integration with base station antennas in wireless communication systems. In this study, three techniques for the miniaturization of a Rotman lens, i.e., Chebyshev impedance transformers, power dividers, and truncated ports with energy distribution slots, are introduced to design the Rotman lens to reduce the size of the ports and hence the total area occupied by the Rotman lens. Simulation and measurement results indicate that good impedance matching between the lens body and its feed lines can be achieved. Using the proposed truncated ports with energy distribution slots, the size of the Rotman lens can be greatly reduced without performance degradation or production cost increment. Moreover, two possible applications of the proposed miniaturized Rotman lens to wireless communication systems are investigated. Rotman lens can not only provide multiple phase difference signals along the array ports to realize multibeams, but also generate high-performance formed beams such as flat-topped radiation pattern.

Key words: Rotman lens; Miniaturization; Multibeam; Beamformer; Wireless communication
https://doi.org/10.1631/FITEE.1900501 **CLC number:** TN819.1

1 Introduction

Due to the rapid development of wireless communication, passive beam formers have received increased attention in the last two decades (Cheng et al., 2010; Lee et al., 2010; Sun et al., 2018). Among these beam formers, Rotman lens is a conventional and versatile device with many advantages, such as true-time delay (TTD) characteristic, multibeam capability, and wide bandwidth. Thus, Rotman lens has been used in a wide range of applications in wireless communication systems (Rotman and Turner, 1963).

Rotman lenses exhibiting improved performance have been investigated in terms of insertion loss improvement (Schulwitz and Mortazawi, 2008), reduction of conjugate port coupling (Ibbotson et al., 2013), and minimum phase-error performance (Darvazehban et al., 2017). However, the conventional Rotman lens has a considerably large size, which is prone to cause difficulties on its integration with base station antennas in wireless communication systems. Therefore, the reduction of the area occupied by a Rotman lens without performance degradation or production cost increment is of particular importance.

Traditional Rotman lens is composed mainly of two parts, i.e., lens body and lens ports. The lens body is shaped of a focal arc and an inner lens contour. The beam and array port locations are designed according to the typical lens equations proposed by Rotman and Turner (1963). The size of the lens body is relatively

‡ Corresponding author
ORCID: Bao-hua SUN, https://orcid.org/0000-0003-1237-5363; Qiu-yan LIANG, https://orcid.org/0000-0002-2553-6173; Gao-nan ZHOU, https://orcid.org/0000-0003-4867-5763

constant to ensure the phase relationship of the Rotman lens (Hansen, 1991). Traditional Rotman lens uses linearly tapered transitions as lens ports. These transitions have been analyzed by Musa and Smith (1989) and Attaran et al. (2016). The value of the flare angle $\theta \leq 12.5°$ has been verified to be a reasonable choice for triangular transition design, thus resulting in the large size of the lens ports. Several methods have been proposed to reduce the size of the Rotman lens, such as folding Rotman lens along the middle plane (Vo Dai et al., 2017), folding Rotman lens using the substrate integrated waveguide (SIW) technology (Tekkouk et al., 2016), and wrapped Rotman lens using a special conformal substrate (Vo Dai and Kilic, 2016).

In this study, three miniaturized Rotman lens structures for wireless communication applications, i.e., Rotman lens using Chebyshev impedance transformers, Rotman lens using power dividers, and Rotman lens using rectangular energy distribution slots, are proposed. The operating mechanisms and obtained performance of these miniaturized Rotman lenses are described in detail. Furthermore, some applications of these miniaturized Rotman lenses to wireless communication are discussed.

2 Rotman lens with Chebyshev impedance transformers

2.1 Geometry and principle of the Rotman lens

The layout of a Rotman lens with Chebyshev impedance transformers is illustrated in Fig. 1. The Rotman lens is composed of a lens body and Chebyshev impedance transformers (Liang et al., 2018). These transformers constitute beam ports, array ports, and dummy ports of the Rotman lens. The Rotman lens has four beam ports (B1–B4), seven array ports (A1–A7), and six dummy ports (D1–D6). The beam ports are located along the focal arc and are used to determine the beam directions. The dummy ports are located at the two sides of the lens body to absorb waves reflected from the array ports. The array ports are located along the inner lens contour and serve to achieve the corresponding path length differences. Parameters of the design of the Rotman lens are shown in Table 1.

The optical principle of the Rotman lens is shown in Fig. 2. The array fed by the Rotman lens can simultaneously form multiple beams according to the differences of the desired path lengths. There are physical length differences from the excited beam port to each array port. Therefore, a set of phase difference signals can be obtained at the array ports, which can be used to realize beam scanning in a certain direction. There are four sets of phase differences corresponding to four beam ports. These four sets of phase differences can be used to realize four beams.

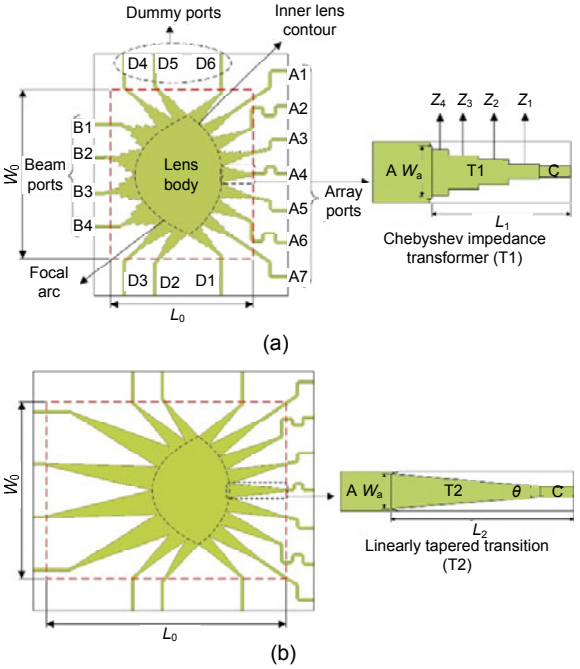

Fig. 1 Layout of the proposed Rotman lens using Chebyshev impedance transformers with W_a=0.6λ_g and L_1=1.2λ_g (a) and W_a=0.6λ_g and L_2=2.3λ_g (b)

Table 1 Parameters of the design of the Rotman lens

Parameter	Value	Parameter	Value
Frequency	10 GHz	Substrate material	Rogers 4350
Beam directions	±10° and ±30°	Substrate thickness	0.762 mm
Element space	18 mm		

The Chebyshev impedance transformer, lens body, and feed line are represented by T1, A, and C, respectively. The lens body and feed line can be matched through the Chebyshev impedance transformer. The Chebyshev impedance transformer consists of multi-section transmission lines with different characteristic impedances.

For comparison, the traditional Rotman lens using linearly tapered transitions is shown in Fig. 1b. The linearly tapered transition (represented by T2) is defined by the flare angle θ. In the conventional Rotman lens, a linearly tapered transition serves as an impedance transformer between the feed line and the aperture of the parallel-plate region due to its ease of fabrication. The reflection coefficient of the linearly tapered transition is affected by the flare angle of the linear transition and the width of the port. The linearly tapered transition should satisfy certain geometric constraints to achieve low return loss. The flare angle of 12.5° and the aperture size λ are reasonable choices for port design of the Rotman lens.

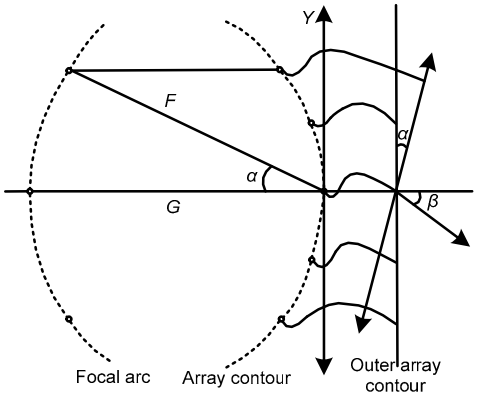

Fig. 2 Optical principle of the Rotman lens

A triangular physical geometry taper is shown in Fig. 1b. Considering the case of the beam port BP2, the length of the beam port (L_{BP2}) can be calculated as

$$L_{BP2}=\frac{W_{BP2}-W_{Z0}}{2\tan(\theta/2)}, \tag{1}$$

where W_{BP2} is the aperture width of the linearly tapered transition, W_{Z0} the width of the feed line, and θ the flare angle of the linearly tapered transition. The value of the aperture width W_{BP2} of the beam port is equal to the value of the waveguide wavelength λ_g, and the flare angle θ of the linearly tapered transitions is 12.5°; that is, $W_{BP2}=\lambda_g$ and θ=12.5°. Then, Eq. (1) can be written as

$$L_{BP2}=\frac{\lambda_g-W_{Z0}}{2\tan 6.25}. \tag{2}$$

The linearly tapered transition has a large electrical size. In the proposed structure (Fig. 1a), all the ports of the Rotman lens are composed of multi-section Chebyshev impedance transformers. When multi-section Chebyshev impedance transformers are used instead of the linearly tapered transitions of the traditional Rotman lens, the length of the ports of the proposed Rotman lens becomes smaller. The area occupied by the proposed Rotman lens is effectively reduced. The Chebyshev impedance transformers provide good matching between the feed lines and the parallel-plate region over a frequency band.

2.2 Analysis of the Chebyshev impedance transformer

Given the port aperture width W, the aperture characteristic impedance Z can be calculated as

$$Z=\begin{cases}\dfrac{60}{\sqrt{\varepsilon_e}}\ln\left(\dfrac{8d}{W}+\dfrac{W}{4d}\right), & \dfrac{W}{d}\le 1,\\[2ex] \dfrac{120\pi}{\sqrt{\varepsilon_e}\left[\dfrac{W}{d}+1.39+0.67\ln\left(\dfrac{W}{d}+1.44\right)\right]}, & \dfrac{W}{d}>1,\end{cases} \tag{3}$$

where d is the thickness of substrate and ε_e is the effect permittivity.

Once the aperture characteristic impedance Z and the characteristic impedance of the feed lines are known, the characteristic impedances of the multi-section transmission lines can be calculated using the small reflection theory (Young, 1962). Detailed design parameters of the Chebyshev impedance transformers are listed in Table 2. Due to the symmetry of the Rotman lens, only the parameters for half of the ports are listed.

Table 2 Parameters of the Chebyshev impedance transformers

Port	W/λ_g	N	Z1 (Ω)	Z2 (Ω)	Z3 (Ω)	Z4 (Ω)
B1	1.0	3	40.1	30.0	10.9	–
B2	1.0	3	40.1	30.0	10.9	–
A1	0.6	4	45.9	33.3	20.9	15.2
A2	0.6	4	45.9	33.3	20.9	15.2
A3	0.6	4	45.9	33.3	20.9	15.2
A4	0.5	4	45.9	33.3	20.9	15.2
D1	0.5	3	43.4	28.6	18.8	–
D2	0.5	3	43.4	28.6	18.8	–
D3	0.5	3	43.4	28.6	18.8	–

As shown in Table 3, the traditional Rotman lens for different flare angles is simulated with the ANSYS HFSS 15 electromagnetic simulator. When the value of θ increases from 12° to 36°, the bandwidth (voltage standing wave ratio (VSWR) <1.5:1) of the beam ports reduces and the insertion loss of the beam ports at 10 GHz reduces. Compared with the traditional Rotman lens, the Chebyshev impedance transformer Rotman lens can achieve good matching characteristic between the lens body and feed lines with a short length. The lower insertion loss can be attributed to the smaller path loss of the Chebyshev impedance transformers.

Both the Chebyshev impedance transformers and the linearly tapered transitions (θ=12°) can achieve good matching characteristic between the lens body and feed lines in the X-band. However, the size of the Chebyshev impedance transformer is smaller and its insertion loss is lower than those of the linearly tapered transition (θ=12°) structure. The size reduction achieved by the Chebyshev impedance transformers is about 56% for the Rotman lens.

2.3 Rotman lens prototype and measurement results

An X-band 4×7 Rotman lens using Chebyshev impedance transformers was designed and fabricated. A photograph of the prototype is shown in Fig. 3. The prototype was tested to verify the simulation results. The layout of the proposed Rotman lens was printed on the top layer of a Rogers RO4350 substrate with a relative permittivity of 3.66 and a dielectric loss tangent of 0.004. Measurement and simulation results are presented and discussed in detail.

Measurement and simulation results of the return loss of beam ports B1–B4 are shown in Fig. 4a. Good agreement is observed between the measurement and simulation results. The proposed Rotman lens exhibits a return loss of larger than 15 dB over the frequency range of 8–12 GHz. The isolation between the beam ports (S_{21}, S_{31}, S_{41}, and S_{32}) is shown in Fig. 4b, larger than 15 dB over the frequency range of 8–12 GHz. The measurement and simulation results of the total insertion loss from beam ports B1–B4 to the array ports are shown in Fig. 5a. The measurement and simulation results of the insertion loss from the beam ports to the dummy ports are shown in Fig. 5b. The proposed Rotman lens exhibits low insertion losses at 10 GHz. The measurement results of the amplitude and phase distribution across the array ports of the proposed Rotman lens at 10 GHz are shown in Fig. 6. The proposed Rotman lens exhibits taper amplitude distribution and equal phase differences across the array ports. These distribution results are useful for the reduction of the sidelobe levels of the forming beams.

Radiation pattern is an important parameter of the Rotman lens, which can provide beam direction, angle, and sidelobe level. Using amplitude and phase data, the array pattern can be calculated by the method in Rotman and Turner (1963) at the center frequency of 10 GHz. Simulation results of the radiation patterns of the traditional Rotman lens for different flare angles are shown in Fig. 7a, when port B2 is active. The radiation pattern results of the proposed Rotman lens are shown in Fig. 7b. Compared with the traditional Rotman lens, the sidelobe level of the proposed Rotman lens is lower, indicating that the proposed Rotman lens can realize the electronically controlled beam scanning from −30° to 30° in 20° increment.

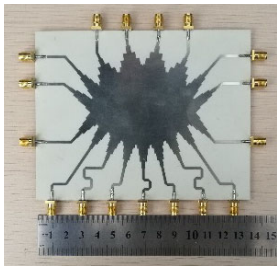

Fig. 3 Fabricated Rotman lens with the Chebyshev impedance transformers

Table 3 Performance comparison of different structures of Rotman lenses

Rotman lens		Bandwidth*		Insertion loss (dB)**		Area (L_0×W_0)
		B1	B2	B1	B2	
Traditional	θ=12°	>40%	>40%	3.2	2.6	$9.6\lambda_g$×$7.2\lambda_g$
	θ=24°	30.4%	>40%	2.6	2.3	$6.3\lambda_g$×$6.0\lambda_g$
	θ=36°	16.1%	29.5%	2.4	2.2	$5.2\lambda_g$×$5.2\lambda_g$
Chebyshev's		>40%	>40%	2.1	1.7	$5.0\lambda_g$×$6.1\lambda_g$

* VSWR<1.5:1. ** At 10 GHz

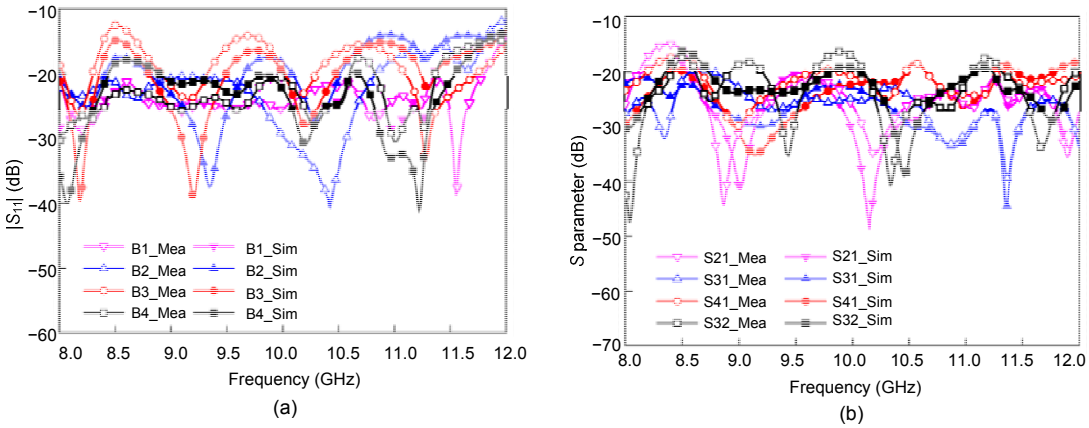

Fig. 4 Simulation and measurement results of *S* parameters: (a) $|S_{11}|$ of beam ports; (b) isolation between beam ports

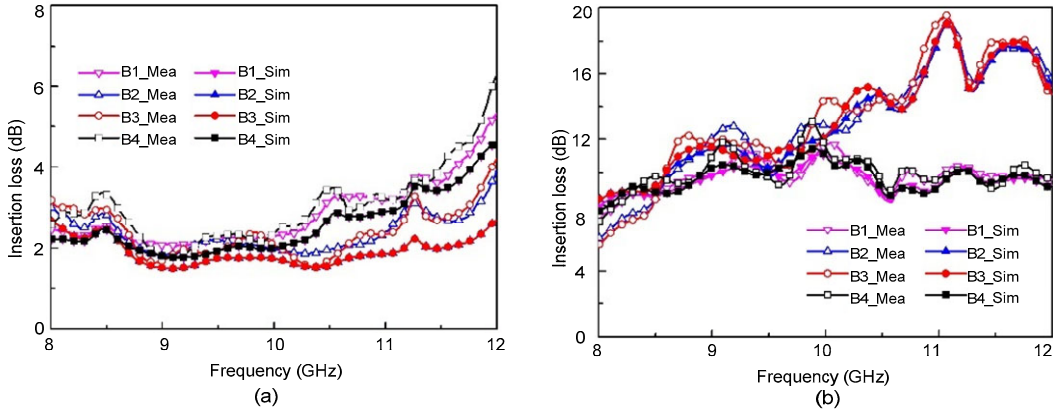

Fig. 5 Total insertion loss: (a) from beam ports to array ports; (b) from beam ports to dummy ports

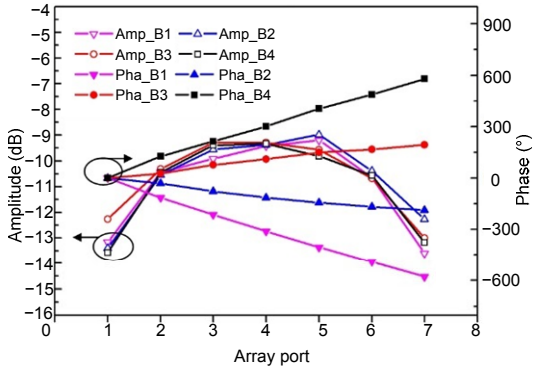

Fig. 6 Measurement results of amplitude and phase distribution across array ports

3 Rotman lens with power dividers

In this section, another technique for the size reduction of a Rotman lens, i.e., Rotman lens with power dividers, is presented.

A 4×8 Rotman lens with power dividers is designed in the frequency range of 1.71–2.17 GHz (Fig. 8). The designed beam directions are ±12° and ±38°. As shown in Fig. 8, 1-to-4 power dividers are connected to the rectangular lens ports. Each 1-to-4 power divider is composed of three 1-to-2 power dividers. The 50-Ω feed line is connected to two 100-Ω transmission lines in parallel. Then, two 100-Ω transmission lines are matched to the 50-Ω transmission lines, which are the sources of the next 1-to-2 power dividers. Since this is a simple validation, only the beam ports employ power dividers and the array ports still use Chebyshev impedance transformers, which are described in Section 2. All the dummy ports are truncated and connected with matching loads to absorb the extra reflected waves.

3.1 Prototype of the Rotman lens with power dividers

A prototype of the Rotman lens with power dividers is shown in Fig. 9. It is designed and fabricated using a Rogers RO4730 substrate with ε_r=3, tan δ=0.0023, and thickness t=1.524 mm. The operating frequency range of the prototype is 1.71–2.17 GHz.

The total size of the prototype is 650 mm×550 mm. Because of the irregular layout of the Rotman lens, it is not easy to obtain the input impedance of the lens port aperture. Thus, the dimensional values for the transmission lines in parallel are obtained using the ANSYS HFSS 15 electromagnetic software.

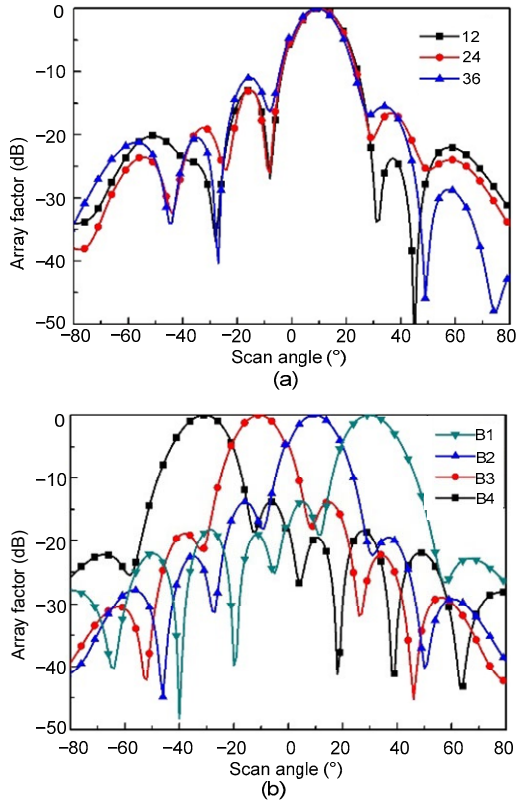

Fig. 7 Radiation patterns of the traditional Rotman lens for different flare angles when port B2 is active (a) and radiation pattern of the proposed Rotman lens (b)

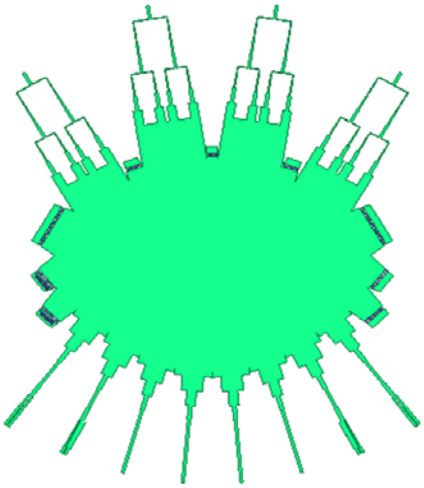

Fig. 8 Layout of the Rotman lens with power dividers

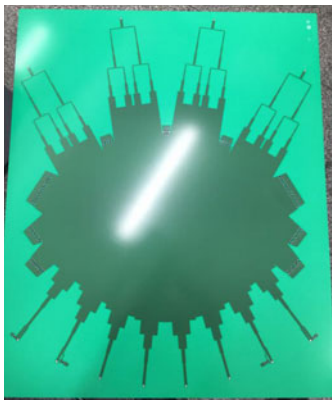

Fig. 9 Fabricated Rotman lens with power dividers

3.2 Simulation and measurement results

The measurement and simulation results of $|S_{11}|$ for the beam ports of the Rotman lens with power dividers are shown in Fig. 10. It can be observed that the VSWR of the beam ports is lower than 1.5:1 over the operating frequency range. Therefore, good independent matching between the feed lines and lens body is achieved. Isolation results between the beam ports are shown in Fig. 11. It can be observed that the isolation between the beam ports is larger than 15 dB in the frequency range of 1.71–2.17 GHz.

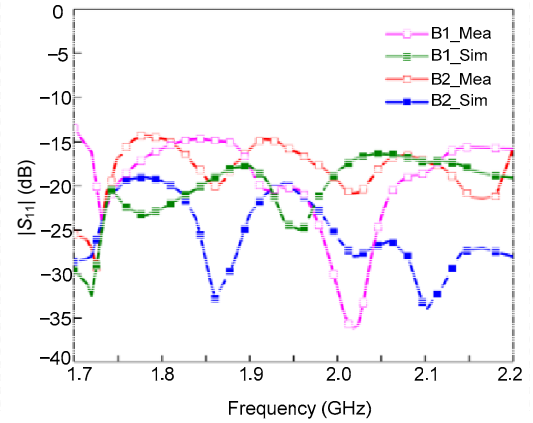

Fig. 10 $|S_{11}|$ results for the beam ports of the Rotman lens with power dividers

The insertion loss results of the Rotman lens are shown in Fig. 12. For a given beam port, the power at each array port is added to find the total power to the array ports. Simulation results indicate that the power ratio at beam ports is larger than 56%, meaning that the Rotman lens exhibits an insertion loss of less than 2.5 dB. From Fig. 12, it can be observed that the

measurement results are worse than the simulation results. This is due to the losses of the lines, copper roughness, and the quality of soldering the subminiature version *A* (SMA) connectors, which are not included in the simulation.

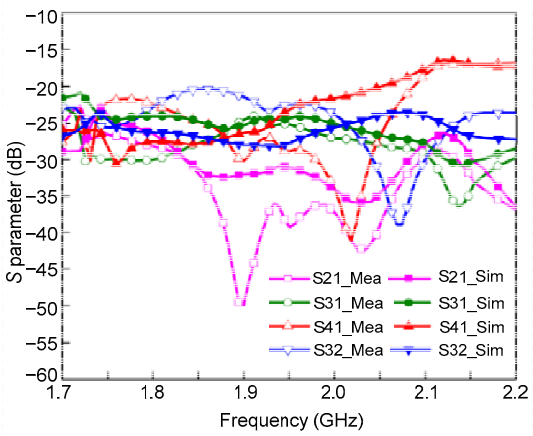

Fig. 11 Isolation results of the Rotman lens with power dividers

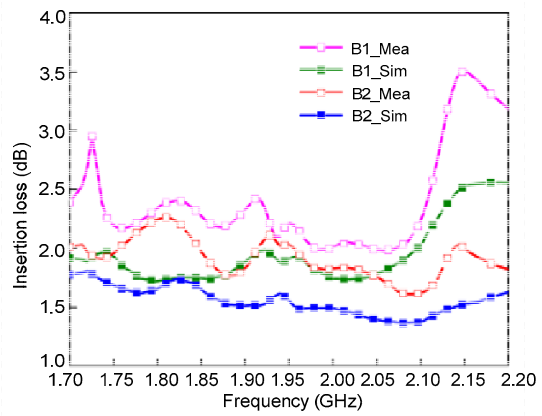

Fig. 12 Insertion loss results of the Rotman lens with power dividers

The beam scanning functions for the Rotman lens with power dividers are validated by measuring the radiation pattern of an antenna array, which is fed by the Rotman lens with power dividers. Results are presented in Fig. 13. The simulated radiation patterns are calculated from the simulated amplitude and phase data of the array ports of the Rotman lens. For comparison between the simulation and measurement results, detailed radiation pattern performances of the Rotman lens are listed in Table 4. A good agreement can be observed between the simulated and measured radiation patterns. In the operating frequency range, the sidelobe levels are lower than −15 dB.

4 Rotman lens using truncated ports with energy distribution slots

An even more miniaturized Rotman lens based on the above mentioned studies (Liang et al., 2018, 2019) is described in this section. Truncated ports connected with energy distribution slots are used. The structure of the proposed miniaturized Rotman lens is depicted in Fig. 14. The proposed Rotman lens is composed of a lens body and several truncated ports connected with energy distribution slots. When a beam port is fed, the electromagnetic wave from the excited beam port such as port B2 flows in the lens body and reaches the array ports (Fig. 15d). The lens port consists of two parts, i.e., a truncated port with a very short length and an energy distribution slot. The distribution slot is placed at the center position of every aperture and at equal distances from both sides. The divider slot modifies the structure of the lens port by dividing the truncated port into two parallel

Table 4 Comparison results of the simulated and measured radiation patterns

Frequency (GHz)	Beam direction (°)				SLL (dB)			
	BP1		BP2		BP1		BP2	
	Sim	Mea	Sim	Mea	Sim	Mea	Sim	Mea
1.71	37	37	12	12	−15.8	−15.5	−20.0	−19.6
1.75	38	38	12	13	−18.7	−19.0	−20.2	−19.8
1.80	38	38	12	12	−17.7	−19.6	−19.4	−18.9
1.90	39	39	12	12	−20.3	−20.8	−19.3	−19.9
1.94	40	39	12	12	−20.0	−21.3	−19.8	−19.7
2.00	40	38	11	11	−19.5	−19.6	−20.6	−20.9
2.17	38	37	12	11	−22.1	−18.8	−24.9	−24.7

Sim: simulation; Mea: measurement. SLL: side lobe level

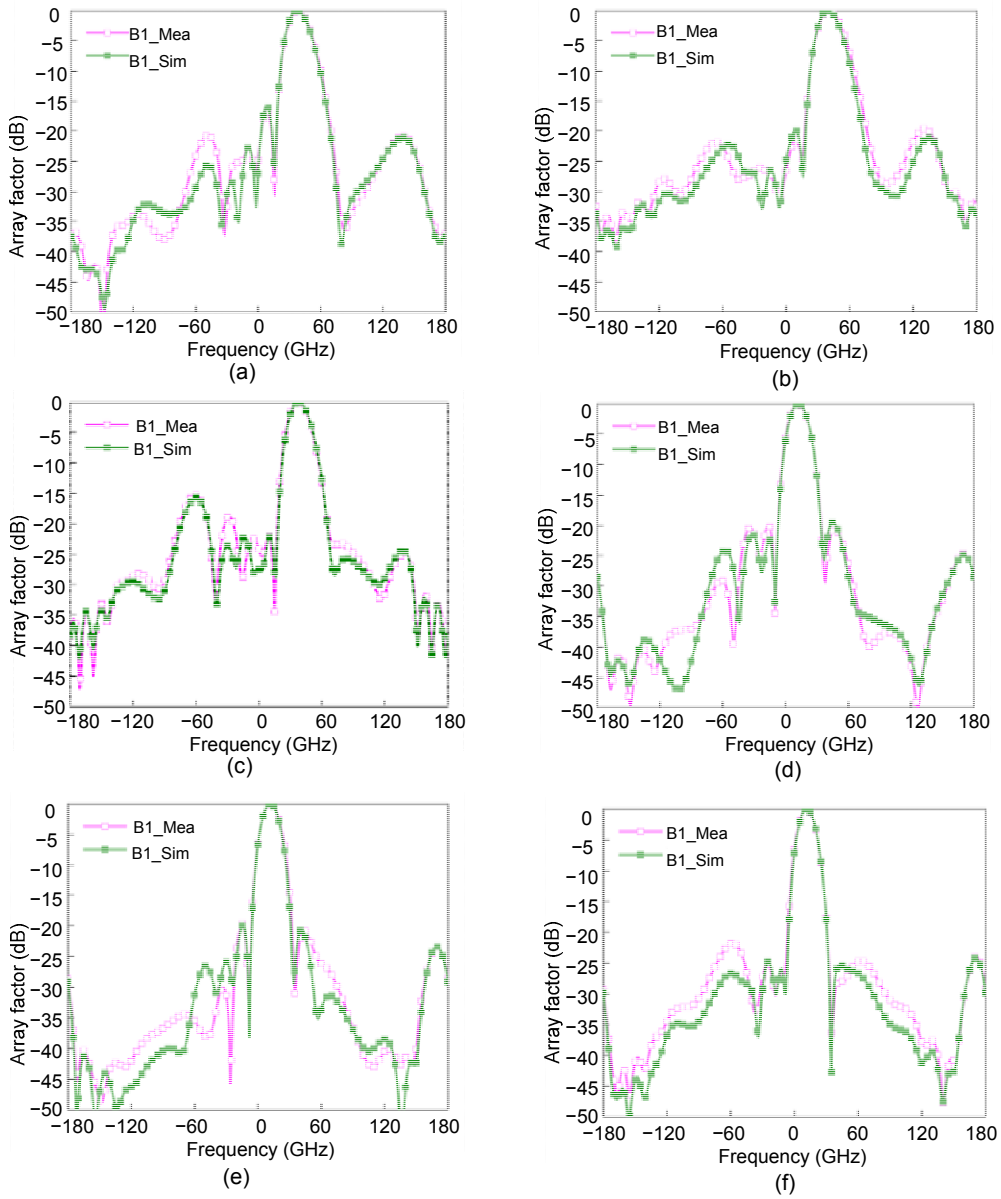

Fig. 13 Radiation pattern results of the Rotman lens with power dividers: (a) port B1 at 1.71 GHz; (b) port B1 at 1.94 GHz; (c) port B1 at 2.17 GHz; (d) port B2 at 1.71 GHz; (e) port B2 at 1.94 GHz; (f) port B2 at 2.17 GHz

transitions. It can be seen from Fig. 14 that the total length of the truncated ports connected with energy distribution slots is smaller than the length of the conventional linearly tapered triangular lens ports. By employing the proposed lens ports, the total size of the 4×7 Rotman lens can be miniaturized from $7.8\lambda_g \times 8\lambda_g$ to $4.8\lambda_g \times 3.3\lambda_g$, thus resulting in significant area reduction. It can be observed that the size of the whole miniaturized Rotman lens is almost equal to the size of its lens body (Fig. 14).

The Rotman lens is mounted on a Rogers RO4350 substrate with ε_r=3.66, tan δ=0.004, and thickness=0.762 mm.

4.1 Evolution steps and discussion

The evolution steps of the miniaturized Rotman lens are direct and clear. They can be divided into three parts. The evolution processes of the miniaturized Rotman lens and the corresponding current propagating simulations are shown in Fig. 15. It can be observed that, when the conventional linearly tapered transition is truncated, a 1-to-2 power divider is

used to connect the lens ports. Subsequently, the short truncated port connected with a 1-to-2 power divider evolves into the final structure of the lens port, which is a compact truncated port connected with energy distribution slots. Detailed descriptions of the three evolution steps are discussed in this section.

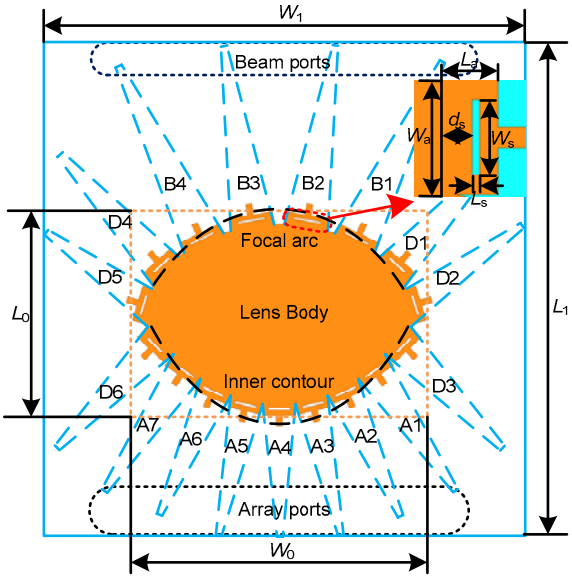

Fig. 14 Miniaturized Rotman lens structure with W_0=4.8λ_g, L_0=3.3λ_g, W_1=7.8λ_g, and L_1=8λ_g
The contour of the conventional Rotman lens is plotted with dotted lines

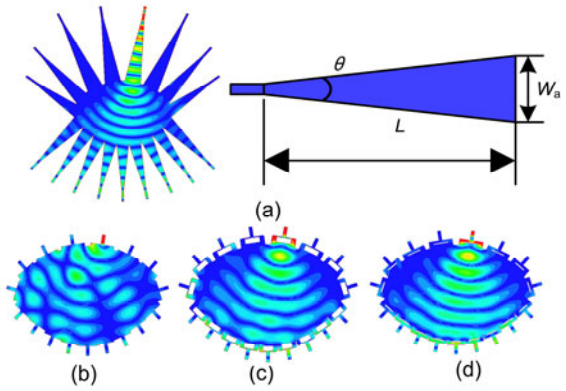

Fig. 15 Current propagation in the lens body with different lens ports when beam port B2 is excited: (a) conventional linearly tapered transition; (b) truncated lens ports; (c) truncated lens ports connected with 1-to-2 power dividers; (d) truncated lens ports connected with energy distribution slots

Step 1: Truncate the linearly tapered transition.

A conventional Rotman lens which uses linearly tapered transitions is shown in Fig. 15a. The flare angle of the linearly tapered transitions is θ=12.5° (Vo Dai and Kilic, 2016) and their length L can be calculated as

$$L=\frac{W_a}{2\tan(\theta/2)}\approx 4.57W_a, \tag{4}$$

where W_a is the base width of the linearly tapered transition. From Eq. (4), it can be observed that the linearly tapered transition occupies quite a large area. A miniaturized Rotman lens using short-truncated lens ports are shown in Fig. 15b. By observing Figs. 15a and 15b, it can be concluded that by employing truncated linearly tapered transitions, the total size of the Rotman lens can be effectively reduced. However, the electromagnetic wave power from the 50-Ω feed line cannot propagate uniformly from the excited lens port to the array ports when the lens port is directly truncated. This happens because the aperture width of the truncated lens port is large, while the width of the 50-Ω feed line is very small. Therefore, a discontinuity impedance problem appears between the 50-Ω feed line and the lens body.

Step 2: Combine truncated ports with power dividers.

To address the discontinuity impedance problem, several 1-to-2 power dividers are used to connect the feed lines and the lens port base (Fig. 15c). A pair of parallel 100-Ω transmission lines is designed to connect the 50 Ω feed line. Next, the pair of 100-Ω transmission lines is connected to the two ends of the lens port base using two matching transitions in parallel. By adjusting the values of the parallel matching transition parameters, continuous impedance matching can be obtained between the feed lines and the lens port base. Simulation results of the propagating current in Fig. 15c indicate that the method of using 1-to-2 power dividers allows a uniform electromagnetic wave power flow from the excited feed lines. The electromagnetic wave power from the excited 50-Ω feed line flows in two parallel matching transitions, and in-phase stacking is obtained at the center location of the lens body base because of the symmetrical structure of the 1-to-2 power divider.

Step 3: Miniaturize power dividers to slots.

A more miniaturized size of the lens ports can be achieved if the lens ports in step 2 are transformed to shorter truncated ports connected with energy divider

slots (Fig. 15d). The ANSYS HFSS 15 software is used to obtain the suitable design parameters for the energy divider slots. The eventual parameter choice of the lens ports is shown in Table 5. Simulation results of the propagating current in Fig. 15d indicate that the electromagnetic wave power from the excited beam port B2 flows smoothly into the lens body and array ports.

Table 5 Parameters of the lens ports (unit: mm)

Port	W_a	L_a	W_s	L_s	D_s
B1	11.4	2.6	6.7	0.5	0.9
B2	11.4	2.8	7.1	0.5	1.2
A1	9.4	2.4	6.2	0.6	0.5
A2	8.9	2.7	5.7	0.6	0.8
A3	8.6	2.9	5.7	0.6	1.0
A4	8.6	3.1	5.7	0.6	1.2
D1	9.6	2.4	5.5	0.6	0.5
D2	9.5	2.4	5.5	0.6	0.5
D3	9.5	2.4	5.1	0.6	0.5

Four different Rotman lenses with different lens port structures are simulated, and the results of the return loss are presented in Fig. 16 when beam port B2 is excited. The first one is the Rotman lens with linearly tapered transitions. The linearly tapered transitions exhibit a slow width change. The best results of return loss were achieved by Musa and Smith (1989). The second one is the Rotman lens with short-truncated ports, whose structure exhibits a sharp width change, and thus the discontinuity impedance problem appears (Fig. 16). The third one is the Rotman lens with power dividers. A cushioning process is provided for the electromagnetic wave power flowing from the excited feed lines, so continuous impedance matching is obtained compared with the previous two lenses. The last one is the Rotman lens with energy divider slots. Based on the contribution of the power dividers, good impedance matching is obtained, although the return loss bandwidth is not as wide as that in the Rotman lens with power dividers because of the larger miniaturized size.

4.2 Simulation and measurement results

To verify the proposed method, a 4×7 Rotman lens with compact truncated ports connected with rectangular energy divider slots is designed and fabricated for the X-band operation (Fig. 17). The Rotman lens characteristics are measured to demonstrate its performance. Simulation and measurement results are shown in Figs. 18–21. SMA connectors are used for all ports except the port under test.

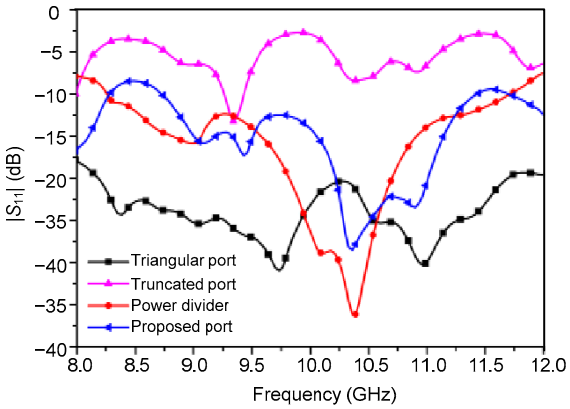

Fig. 16 $|S_{11}|$ of a Rotman lens with different lens ports when port B2 is excited

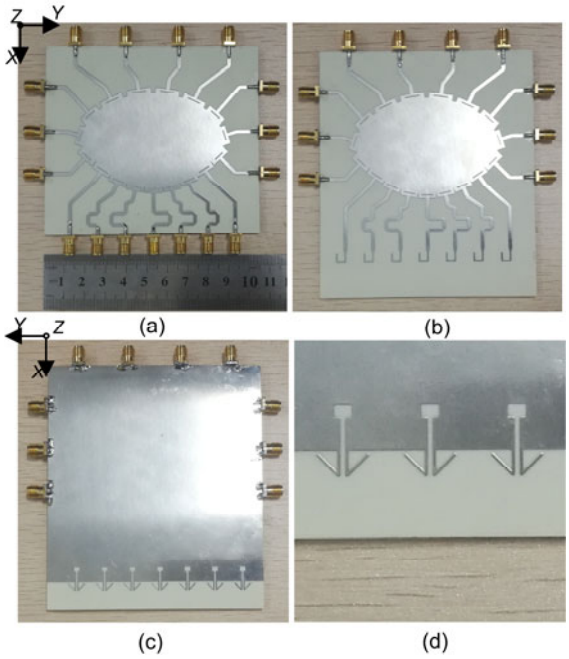

Fig. 17 Rotman lens and array: (a) Rotman lens; (b) Rotman lens with antenna array (top); (c) Rotman lens with antenna array (bottom); (d) antenna array

To ensure that the energy from the excited beam port can be transmitted efficiently to the array port apertures, low return loss is required. $|S_{11}|$ simulation and measurement results of the four beam ports are given in Fig. 18. The return losses observed are similar for all ports. The designed Rotman lens exhibits a

27% impedance matching bandwidth (VSWR<2:1) in the frequency range of 8.73–11.42 GHz, indicating that good matching between the lens body and feed lines can be obtained using lens ports with energy distribution slots.

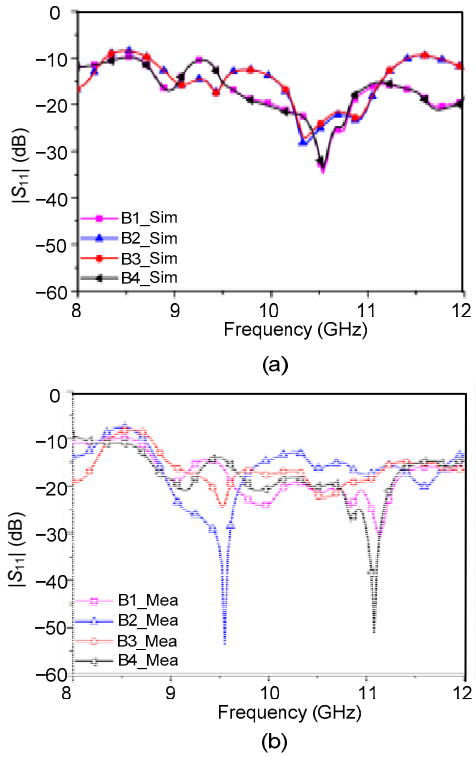

Fig. 18 $|S_{11}|$ of the beam ports: (a) simulation results; (b) measurement results

Simulation and measurement results of the isolation between the beam ports are presented in Fig. 19. Because of the symmetrical structure of the Rotman lens, only the scattering parameters S_{12}, S_{13}, S_{14}, and S_{23} are shown. It can be observed that the isolation between beam ports is larger than 17.2 dB.

Simulation and measurement results of the insertion loss for every beam port are presented in Fig. 20. A certain distance between the SMA connectors must be kept for measurements. For this purpose, feed and delay lines with relatively large lengths are used, resulting in about 0.58-dB and 0.74-dB losses for beam ports B1 and B2 at 10 GHz, respectively. Simulation results of the insertion loss after de-embedding the extra insertion loss are presented in Fig. 20. It can be observed that the proposed compact Rotman lens exhibits low insertion loss of 2.19 dB for beam port B1 and 1.48 dB for beam port

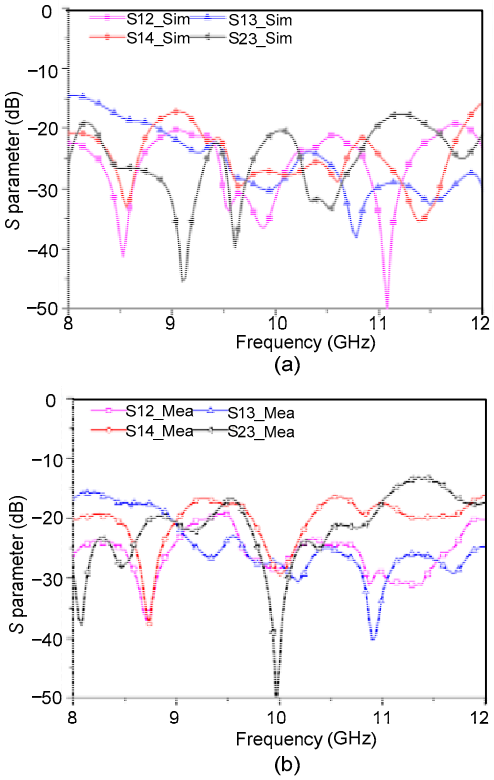

Fig. 19 Isolation results of beam ports: (a) simulation results; (b) measurement results

B2 at 10 GHz. The results indicate that the measured insertion losses are larger than the simulated ones at high frequencies. This can be attributed to the bandwidth performance limitation of the SMA connectors.

To verify the beam scanning function of the Rotman lens, a broadband printed-dipole array (Ta et al., 2017) is used. Delay lines are used between the antenna array and the Rotman lens (Fig. 17). The normalized simulation and measurement results of radiation patterns at 9, 10, and 11 GHz are shown in Fig. 21 for the four beam ports. Similar results are observed for all the four ports. The beam direction ranges from −33° to 33° in 11° increment. As predicted, the beam direction angles remain constant because of the TTD characteristics of Rotman lens.

Three Rotman lenses proposed by Musa and Smith (1989), Tekkouk et al. (2016), and Liu et al. (2018) are compared with the proposed compact Rotman lens. Details and performances of each Rotman lens are listed in Table 6. It is evident that the proposed compact Rotman lens exhibits a considerable size reduction. Other advantages of the proposed Rotman lens are easy processing, wide bandwidth, and low cost.

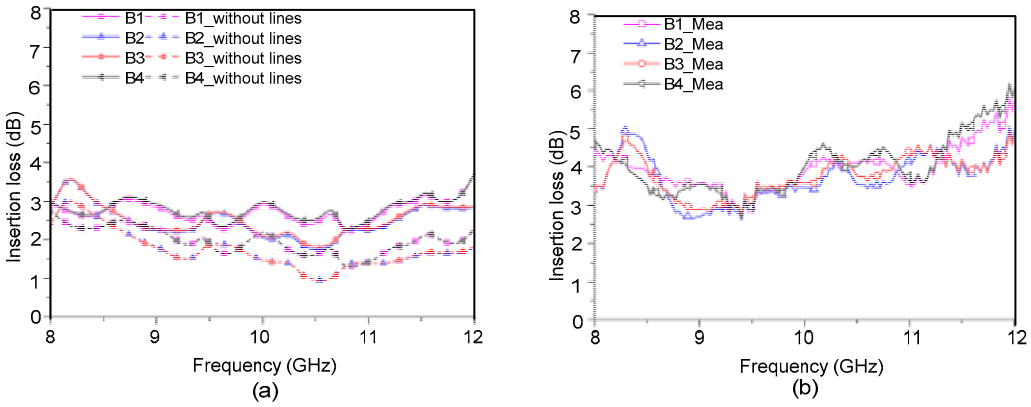

Fig. 20 Insertion loss results of beam ports: (a) simulation results; (b) measurement results

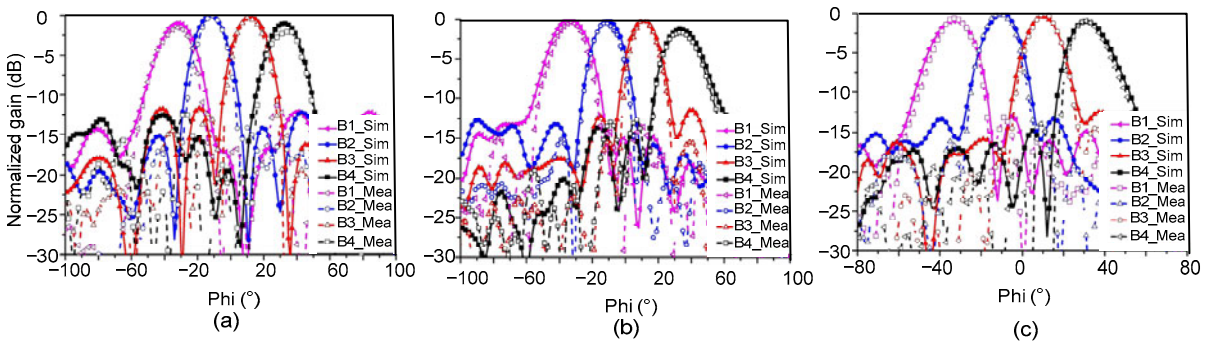

Fig. 21 Simulation and measurement results of the normalized radiation patterns at 9 GHz (a), 10 GHz (b), and 11 GHz (c)

Table 6 Comparison between our work and other works on Rotman lenses

Reference	Number of ports (BP×AP)	Size	Number of layers	Bandwidth
Tekkouk et al. (2016)	5×15	$17.9\lambda_g \times 10.7\lambda_g$	2	4.1%
Liu et al. (2018)	6×8	$15.9\lambda_g \times 5.6\lambda_g$	2	14.3%
Musa and Smith (1989)	5×5	$6.2\lambda_g \times 4.1\lambda_g$	1	7.0%
This paper	4×7	$4.8\lambda_g \times 3.3\lambda_g$	1	26.9%

BP: beam port; AP: array port

5 Applications of miniaturized Rotman lenses to wireless communication

With the rapid development of mobile electronic devices, there has been a growing demand for high data rates in wireless communication systems. The traditional directional signal-beam antennas cannot achieve omnidirectional coverage in some scenarios, such as in public squares and neighborhoods. Complete signal coverage can be achieved by employing a multibeam system with beam scanning functions. Multibeam technology is a signal processing technique which directs a signal to the desired direction. This technology has been widely used to increase the coverage of wireless communication systems and guarantee high quality of service to the subscribers.

At present, there are three main techniques to achieve multibeam transmission, i.e., reflector antennas, phased-array antennas, and passive beam forming. The reflector antennas have the characteristics of high gain, simple structure, and beam scanning, which can be easily realized. However, due to the limitation of the feed-source position and the structure of the reflection surface, beams formed by the reflector antennas have a considerable difference and the number of scanning beams is small. The phased-array multibeam antennas require electronic components, their processing is complex, and their cost is

high. Passive beam formers offer several advantages due to their multibeam capabilities and high capacity. Butler matrix and Rotman lens are commonly known key components for feeding multibeam antenna arrays. Compared with the Butler matrix, the Rotman lens exhibits TTD characteristic, which is of significant importance in wireless communication. Two possible multibeam applications of the Rotman lens are shown in Fig. 22a. The beam ports are connected to the signal generators, and the array ports are connected to the antenna array. When the beam ports are excited, multiple signals of different phases can be generated. As mentioned in Sections 2–4, the radiation patterns in Figs. 7, 13, and 21 show that multibeam systems fed by a Rotman lens can achieve multibeam characteristics within a coverage area.

As illustrated in Fig. 22b, another application of the Rotman lens is to produce a flat-topped radiation pattern (FTRP) (Zhang et al., 2012). For an efficient wireless communication service, it is important to radiate electromagnetic waves of uniform amplitude within the service area and suppress the sidelobe levels. For this purpose, short-range wireless communication antennas are required to provide an FTRP with "limited field of view" type characteristics (Mailloux, 1993; Skobelev, 1998; Eom et al., 2008). Generally, lens antennas, leaky-wave antennas, and phased-array antennas are used to produce an FTRP (Mailloux, 1993; Nguyen et al., 2011; Scattone et al., 2015). However, the phased-array antenna system requires multiple radio frequency (RF) chains, phase shifters, and analog-to-digital converters, which are expensive and energy consuming (Mailloux, 1993) components. Lens antennas and leaky-wave antennas are limited in terms of bandwidth and cost, especially in the millimeter-wave band (Nguyen et al., 2011; Scattone et al., 2015). The Rotman lens provides a competitive candidate to produce an FTRP due to its TTD and low-profile characteristics.

To produce an FTRP, the beam ports of the Rotman lens should be simultaneously excited (Fig. 22b). When multiple beam ports are excited at the same time, the energy received by the array ports is the vector superposition from various beam ports. In this case, the amplitudes and phases of each array port are symmetrically tapered, thus meeting the excitation requirements of the produced FTRP.

A Rotman lens with nine beam ports is designed to produce an FTRP. The radiation patterns of the FTRP are shown in Fig. 23. When nine beam ports are simultaneously excited, the FTRP has a 3-dB beam width of 74.7° and a side lobe level (SLL) of −27.9 dB. When seven beam ports are simultaneously excited, the FTRP has a 3-dB beam width of 58.3° and an SLL of −20.9 dB. When five beam ports are simultaneously excited, the FTRP has a 3-dB beam width of 41.9° and an SLL of −23.8 dB. If only one beam port is excited, the produced beam will become a pencil beam. Therefore, it is concluded that a wider FTRP beam width can be achieved by exciting more beam ports.

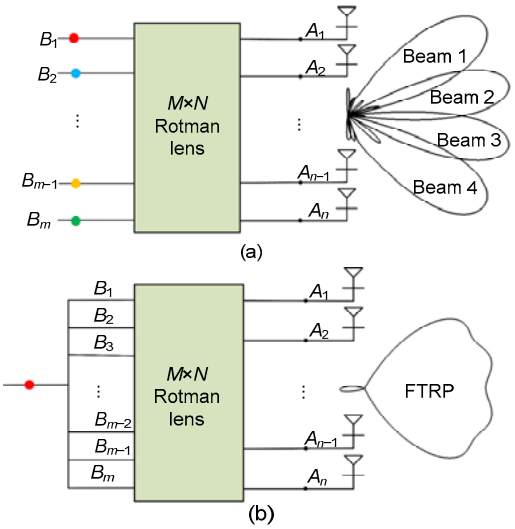

Fig. 22 Two application cases of the Rotman lens: (a) case 1 (multibeam); (b) case 2 (flat-topped radiation pattern, FTRP)

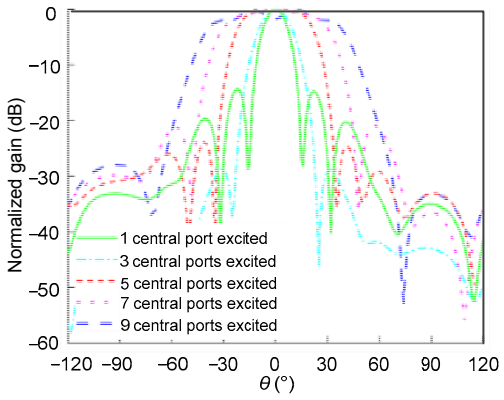

Fig. 23 Flat-topped radiation patterns

6 Conclusions and future work

In this work, three techniques have been investigated for the miniaturization of Rotman lens

structures for wireless communication applications. Chebyshev impedance transformers, power dividers, and truncated lens ports with energy divider slots have been introduced to the design of the Rotman lens. These techniques result in a more compact port layout, and hence a reduced overall size of the Rotman lens. Simulation and measurement results indicated that good impedance matching between the lens body and feed lines can be achieved. It is noted that using the proposed truncated lens ports with the energy divider slot structure, the layout of the Rotman lens becomes more compact without performance degradation or production cost increment. Therefore, a robust technique for the miniaturization of the Rotman lens has been demonstrated.

The Rotman lens, when used as a passive beam former, can not only provide multiple phase difference signals along array ports to realize multibeams, but also generate formed beams with high performance such as an FTRP. The Rotman lens provides a good candidate for passive beam formers and has many potential applications in future wireless communication systems.

Contributors

Bao-hua SUN and Qiu-yan LIANG designed the research. Qiu-yan LIANG wrote the first draft. Bao-hua SUN and Gao-nan ZHOU helped organize the manuscript. Bao-hua SUN and Gao-nan ZHOU revised and edited the final version.

Compliance with ethics guidelines

Bao-hua SUN, Qiu-yan LIANG, and Gao-nan ZHOU declare that they have no conflict of interest.

References

Attaran A, Rashidzadeh R, Kouki A, 2016. 60 GHz low phase error Rotman lens combined with wideband microstrip antenna array using LTCC technology. *IEEE Trans Antenn Propag*, 64(12):5172-5180. https://doi.org/10.1109/TAP.2016.2618479

Cheng YJ, Hong W, Wu K, 2010. Design of a substrate integrated waveguide modified R-KR lens for millimetre-wave application. *IET Microw Antenn Propag*, 4(4):484-491. https://doi.org/10.1049/iet-map.2008.0379

Darvazehban A, Manoochehri O, Ali Salari M, et al., 2017. Ultra-wideband scanning antenna array with Rotman lens. *IEEE Trans Microw Theory Techn*, 65(9):3435-3442. https://doi.org/10.1109/TMTT.2017.2666810

Eom SY, Kim SK, Yook JG, 2008. Multilayered disk array structure surrounded by a dielectric ring for shaping a flat-topped radiation pattern. *IEEE Antenn Wirel Propag Lett*, 7:374-376. https://doi.org/10.1109/LAWP.2008.2001631

Hansen RC, 1991. Design trades for Rotman lenses. *IEEE Trans Antenn Propag*, 39(4):464-472. https://doi.org/10.1109/8.81458

Ibbotson A, de Villiers DIL, Palmer KD, 2013. A defocused Rotman lens with reduced conjugate port coupling. *IEEE Microw Wirel Compon Lett*, 23(8):394-396. https://doi.org/10.1109/LMWC.2013.2268455

Lee W, Kim J, Cho CS, et al., 2010. Beamforming lens antenna on a high resistivity silicon wafer for 60 GHz WPAN. *IEEE Trans Antenn Propag*, 58(3):706-713. https://doi.org/10.1109/TAP.2009.2039331

Liang QY, Zhou GN, Sun BH, et al., 2018. Compact microstrip Rotman lens using Chebyshev impedance transformers. *Progr Electromag Res Lett*, 76:1-6.

Liang QY, Sun BH, Zhou GN, et al., 2019. Design of compact Rotman lens using truncated ports with energy distribution slots. *IEEE Access*, 7:120766-120773. https://doi.org/10.1109/ACCESS.2019.2925000

Liu Y, Yang H, Jin ZS, et al., 2018. Compact Rotman lens-fed slot array antenna with low sidelobes. *IET Microw Antenn Propag*, 12(5):656-661. https://doi.org/10.1049/iet-map.2017.0466

Mailloux RJ, 1993. Phased Array Antenna. Artech House, London, UK.

Musa L, Smith MS, 1989. Microstrip port design and sidewall absorption for printed Rotman lenses. *IEE Proc H Microw Antenn Propag*, 136(1):53-59. https://doi.org/10.1049/ip-h-2.1989.0009

Nguyen NT, Sauleau R, Le Coq L, 2011. Reduced-size double-shell lens antenna with flat-top radiation pattern for indoor communications at millimeter waves. *IEEE Trans Antenn Propag*, 59(6):2424-2429. https://doi.org/10.1109/TAP.2011.2144554

Rotman W, Turner RF, 1963. Wide-angle microwave lens for line source applications. *IEEE Trans Antenn Propag*, 11(6):623-632. https://doi.org/10.1109/TAP.1963.1138114

Scattone F, Ettorre M, Sauleau R, et al., 2015. Optimization procedure for planar leaky-wave antennas with flat-topped radiation patterns. *IEEE Trans Antenn Propag*, 63(12):5854-5859. https://doi.org/10.1109/TAP.2015.2479242

Schulwitz L, Mortazawi A, 2008. A new low loss Rotman lens design using a graded dielectric substrate. *IEEE Trans Microw Theory Techn*, 56(12):2734-2741. https://doi.org/10.1109/TMTT.2008.2006802

Skobelev SP, 1998. Methods of constructing optimum phased-array antennas for limited field of view. *IEEE Antenn Propag Mag*, 40(2):39-50.

https://doi.org/10.1109/74.683541

Sun L, Zhang GX, Sun BH, 2018. Method of synthesizing orthogonal beam-forming networks using QR decomposition. *IEEE Access*, 7:325-331. https://doi.org/10.1109/ACCESS.2018.2885358

Ta SX, Choo H, Park I, 2017. Broadband printed-dipole antenna and its arrays for 5G applications. *IEEE Antenn Wirel Propag Lett*, 16:2183-2186. https://doi.org/10.1109/LAWP.2017.2703850

Tekkouk K, Ettorre M, Le Coq L, et al., 2016. Multibeam SIW slotted waveguide antenna system fed by a compact dual-layer Rotman lens. *IEEE Trans Antenn Propag*, 64(2): 504-514. https://doi.org/10.1109/TAP.2015.2499752

Vo Dai TK, Kilic O, 2016. Compact Rotman lens structure configurations to support millimeter wave devices. *Progr Electromag Res B*, 71(1):91-106. https://doi.org/10.2528/PIERB16082704

Vo Dai TK, Nguyen T, Kilic O, 2017. A compact microstrip Rotman lens design. United States National Committee of National Radio Science Meeting, p.1-2. https://doi.org/10.1109/USNC-URSI-NRSM.2017.7878311

Young L, 1962. Stepped-impedance transformers and filter prototypes. *IRE Trans Microw Theory Techn*, 10(5):339-359. https://doi.org/10.1109/TMTT.1962.1125523

Zhang Y, Christie S, Fusco VF, et al., 2012. Reconfigurable beam forming using phase-aligned Rotman lens. *IET Microw Antenn Propag*, 6(3):326-330. https://doi.org/10.1049/iet-map.2011.0379